INTERNATIONAL JOURNAL FOR NUMERICAL METHODS IN FLUIDS
Int. J. Numer. Meth. Fluids **30**: 19–42 (1999)

THE ONSET OF THREE-DIMENSIONALITY IN AN OSCILLATING FLOW PAST A FIXED CIRCULAR CYLINDER

JIANFENG ZHANG[1] AND CHARLES DALTON*
Department of Mechanical Engineering, University of Houston, Houston, TX 77204-4792, USA

SUMMARY

A computational study of the sinusoidally oscillating flow past a fixed circular cylinder has been performed to examine the viscous transition from 2D to 3D in the wake of the cylinder, i.e., the Honji instability. The primitive variables form of the Navier–Stokes equations was used with the discretization in the form of a combined finite-difference/spectral-method. Numerical results were obtained at a frequency parameter value of 196 and for a range of Keulegan–Carpenter (KC) numbers from 1 to 4. The calculations agreed quite well with experimental results. At $\mathrm{KC}=1$, the wake is 2D; spanwise structures begin to appear at $\mathrm{KC}=2$; separation has occurred by $\mathrm{KC}=3.2$; and the vortex structures have become chaotic by $\mathrm{KC}=4$. Calculated values of the force coefficients also agree extremely well with the experimental values. Copyright © 1999 John Wiley & Sons, Ltd.

1. INTRODUCTION

The flow in the wake of bluff body is 3D, even before it becomes turbulent, at low Reynolds numbers. When the physical problem is an oscillating flow past a fixed circular cylinder, this viscous transition from a 2D flow to a 3D flow is called the Honji instability. This phenomenon was first observed by Honji [1]. Sarpkaya [2], in a penetrating study of the problem, gave the name 'Honji instability' to this viscous transition.

The present study concerns the combined finite-difference/spectral-method calculation of the Honji instability. Specifically, we represent this flow in terms of the 3D primitive-variables form of the Navier–Stokes equations for an incompressible fluid. A fractional-step method is used to advance the solution in time.

The Honji-instability problem has some similarities to the problem of a steady approach flow past a fixed circular cylinder, about which much more is known. For the steady approach flow, the 2D wake vortex structures are unstable to 3D disturbances at a Reynolds number of about 189, where the wake becomes 3D before turbulence develops (see Barkley and Henderson [3]). The understanding of this problem is well-documented in Roshko [4], Hama [5], Williamson [6,7], Thompson *et al.* [8] and numerous others.

For a circular cylinder in a sinusoidally oscillating flow, the governing parameters are the Reynolds number, defined as $Re = U_{\mathrm{m}}d/v$, and the Keulegan–Carpenter number, defined as $\mathrm{KC} = U_{\mathrm{m}}T/d$, where U_{m} is the maximum oscillatory velocity, v is the fluid kinematic viscosity,

---

* Correspondence to: Department of Mechanical Engineering, University of Houston, Houston, TX 77204-4792, USA.
[1] Current address: Halliburton Services, Houston, TX, USA.

CCC 0271–2091/99/090019–28$17.50

Received 3 June 1997
Revised 23 April 1998

T is the period of oscillation and d is the cylinder diameter. A frequency parameter, defined as $\beta = d^2/\nu T = Re/\mathrm{KC}$, is often used to replace the Reynolds number as the second parameter. Sarpkaya [2] has given a detailed discussion of the phenomena associated with this oscillating flow. A brief synopsis is that, at a given value of β, the flow goes through a series of different flow regimes as KC changes. For a given value of β, the flow is 2D and laminar at low KC. As KC increases, a viscous transition to a 3D wake occurs. The next regime, occurring with an increase in the KC value, is that wake turbulence is generated. The final regime is identified as one in which separation has occurred after further increases in KC. In particular, at $\beta = 1035$, we note from Figure 7 in [2] that the transition to a 3D wake (dubbed the Honji instability by Sarpkaya) occurs at $\mathrm{KC} \cong 1.1$, separation occurs at $\mathrm{KC} \cong 1.5$ and transition to turbulence at $\mathrm{KC} \cong 1.9$.

The Honji instability is a 3D vortical instability first discovered by Honji [1]. Honji's experiments showed that, when β is between 50 and 800, the flow becomes 3D when KC is between 1.2 and 2.4. The critical value of KC for the flow to become unstable to 3D disturbances, $\mathrm{KC}_{\mathrm{cr}}$, shows a steeper decrease with increasing β, when β is less than 200. When β exceeds 200, $\mathrm{KC}_{\mathrm{cr}}$ decreases more slowly. When KC is greater than $\mathrm{KC}_{\mathrm{cr}}$, the streak sheets form steady mushroom-like structures on the sides of the cylinder that are perpendicular to the direction of oscillation. These structures have equal spacing along the axial direction, and lie alternatively on the two sides. Honji also observed that, when KC is further increased to be greater than a transitional KC number, KC_{t}, the flow becomes turbulent due to long-standing separation of the Stokes layer (the layer of high vorticity and gradients close to the wall of the cylinder). For the range of β values considered, the difference between KC_{t} and $\mathrm{KC}_{\mathrm{cr}}$ is relatively invariant (between 0.9 and 1.2). Apparently, separation occurs after the Honji instability, at a value of KC between $\mathrm{KC}_{\mathrm{cr}}$ and KC_{t}.

Based on Honji's observation that this instability may be a centrifugal-type instability, Hall [9] assumed it is of the Taylor–Görtler-type, and made a linear stability analysis of the 2D flow for the limiting case of very large β and very small KC. The analysis was further simplified from the conclusion that the flow is most unstable at the points to which the radial lines are perpendicular to the direction of oscillation. Finally, Hall was able to obtain a relation between $\mathrm{KC}_{\mathrm{cr}}$ and β, which shows $\mathrm{KC}_{\mathrm{cr}}$ essentially decreases as $\beta^{-1/4}$. This relation agrees with $\mathrm{KC}_{\mathrm{cr}}$ obtained by Honji.

2. ANALYSIS

2.1. Governing equations

To describe the Honji-instability problem, i.e., the viscous transition from 2D to 3D in an oscillating flow, we use the nondimensional versions of the continuity equation and the Navier–Stokes equation:

$$\nabla \cdot \mathbf{v} = 0 \tag{1}$$

and

$$\frac{1}{2\mathrm{KC}} \frac{\partial \mathbf{v}}{\partial \tau} + (\nabla \times \mathbf{v}) \times \mathbf{v} = -\nabla \Phi + \frac{2}{Re} \nabla^2 \mathbf{v}, \tag{2}$$

where $\mathbf{v}$ is the nondimensional velocity vector scaled by the maximum oscillatory velocity, U_{m}; τ is the nondimensional time, $\tau = t/T$; Re is the Reynolds number defined earlier; and

$\Phi = 2p/\rho U_{\mathrm{m}}^2 + \mathbf{v}\cdot\mathbf{v}/U_{\mathrm{m}}^2$. In the definition of Φ, p is the dimensional pressure and ρ is the density. For the actual computational scheme, we use the cylindrical forms of Equations (1) and (2).

The nondimensional initial conditions for this problem are

$$u(r, \theta, z, 0) = U(0)\left(1 - \frac{1}{r^2}\right)\cos\theta, \tag{3}$$

$$v(r, \theta, z, 0) = -U(0)\left(1 + \frac{1}{r^2}\right)\sin\theta, \tag{4}$$

and

$$w(r, \theta, z, 0) = 0, \tag{5}$$

where $U(0)$ is found from the nondimensional free-stream velocity,

$$U(\tau) = U_{\mathrm{m}}\sin(2\pi\tau) \tag{6}$$

and u, v and w are the nondimensional velocity components in the r-, θ- and z-directions respectively.

The boundary conditions on the surface of the cylinder are

$$u(1, \theta, z, \tau) = v(1, \theta, z, \tau) = w(1, \theta, z, \tau) = 0 \tag{7}$$

on $r = 1$, which is the cylinder surface in the nondimensional system. In the circumferential direction, the natural periodic boundary conditions apply,

$$f(r, \theta, z, \tau) = f(r, \theta + 2\pi, z, \tau), \tag{8}$$

where the functional $f(\,)$ refers to all three velocity components and the pressure: u, v, w and p. The boundary conditions in the axial direction are not as straightforward as in the other two directions. We can use periodic conditions in this direction also,

$$f(r, \theta, z, \tau) = f(r, \theta, z + Z, \tau), \tag{9}$$

where $f(\,)$ again refers to all three velocity components and Z is the spanwise wavelength. However, the natural wavelength changes with flow conditions and is unknown, so some judgments are necessary in determining this wavelength. This point will be discussed later. We will also defer discussion of the far-field boundary conditions until after the numerical method is presented.

3. THE NUMERICAL REPRESENTATION

Equations (1) and (2) are discretized using a finite-difference/spectral-method approach. Since two of the co-ordinate directions have periodic boundary conditions, use of the Fourier spectral method brings significantly reduced computational cost to this 3D problem.

3.1. Fractional-step method

The second-order in time fractional-step method is used for time advancement of Equation (2). An intermediate velocity, $\hat{\mathbf{v}}$, is obtained from

$$\frac{1}{2\mathrm{KC}}\frac{\hat{\mathbf{v}}-\mathbf{v}^n}{\Delta\tau}=-\frac{1}{2}(3\mathbf{N}^n-\mathbf{N}^{n-1})+\frac{1}{2}\mathbf{L}^n, \tag{10}$$

where the superscripts refer to the time step, **N** represents the (nonlinear) convective terms and **L** represents the (linear) viscous terms. The intermediate velocity is corrected by pressure to obtain a second intermediate velocity, $\tilde{\mathbf{v}}$, from

$$\frac{1}{2\mathrm{KC}}\frac{\tilde{\mathbf{v}}-\hat{\mathbf{v}}}{\Delta\tau}=-\nabla\Phi^{n+1/2} \tag{11}$$

and

$$\tilde{Q}=\nabla\cdot\tilde{\mathbf{v}}=0. \tag{12}$$

Finally, the velocity at time step $n+1$ is obtained from

$$\frac{1}{2\mathrm{KC}}\frac{\mathbf{v}^{n+1}-\tilde{\mathbf{v}}}{\Delta\tau}=\frac{1}{2}\mathbf{L}^{n+1}. \tag{13}$$

In Equation (11), the pressure head, Φ, is unknown. To determine it, we apply the continuity equation, which must be satisfied at the end of each complete time step. So, we take the divergence of Equation (13) to get Equation (12).

Then, we take the divergence of Equation (11) and apply Equation (12) to get

$$\nabla^2\Phi^{n+1/2}=\frac{1}{2\mathrm{KC}}\frac{\nabla\cdot\hat{\mathbf{v}}}{\Delta\tau}. \tag{14}$$

After $\Phi^{n+1/2}$ is found from Equation (14) and with the solution for $\hat{\mathbf{v}}$ from Equation (10), $\tilde{\mathbf{v}}$ and $\mathbf{v}^{n+1}$ can be calculated from Equations (11) and (13) respectively. No boundary conditions are necessary for either of the two intermediate velocities.

The fractional-step method is an approximation which, in effect, linearizes Equation (2) by evaluating the convective terms at times other than the time at the $n+1$ level. Adding Equations (10), (11) and (13), which are the equations describing the individual steps of the fractional-step method, yields

$$\frac{1}{2\mathrm{KC}}\left(\frac{\mathbf{v}^{n+1}-\mathbf{v}^n}{\Delta\tau}\right)=-\nabla\Phi^{n+1/2}-\frac{1}{2}(3\mathbf{N}^n-\mathbf{N}^{n-1})+\frac{1}{2}(\mathbf{L}^{n+1}+\mathbf{L}^n). \tag{15}$$

Equation (15) represents the advance in time from the n level to the $n+1$ level for the velocity with the right-hand-side representing the pressure, convective and viscous terms at times less than the $n+1$ level.

The divergence-free condition on $\mathbf{v}^{n+1}$ is not automatically satisfied; an extra step must be taken to assure that $\nabla\cdot\mathbf{v}^{n+1}$ is sufficiently small. So, we take the divergence of Equation (13) and use Equation (12) to get

$$\frac{1}{2\mathrm{KC}}\frac{Q^{n+1}}{\Delta\tau}=\frac{1}{Re}\nabla^2Q^{n+1}, \tag{16}$$

which shows that Q^{n+1} satisfies a numerical boundary layer equation [10]. The divergence (Q^{n+1}) is zero only if it is zero on the boundary, especially no-slip boundaries. If not, the divergence will decrease with the normal distance from the boundary proportional to $O((\Delta\tau/Re)^{-1/2})$. The divergence in this numerical boundary can be $O(\Delta\tau)$, whereas the divergence in other parts of the flow field is of the order $O(\Delta\tau^2)$. This could lead to large divergences or inaccurate solutions for some problems, especially if the solution for pressure needs to be accurate near solid walls, such as when fluid forces are of interest. Therefore, careful attention must be paid to the value of Q^{n+1} and the time and space steps may have to be modified to get acceptably low values of the divergence.

To control this time-splitting error, we use the consistent scheme developed by Karniadakis *et al.* on boundary conditions for pressure on no-slip solid boundaries,

$$\frac{\partial \Phi}{\partial n} = -\frac{2}{Re}\,\mathbf{n}\cdot\nabla\times(\nabla\times\mathbf{v}), \tag{17}$$

where n refers to the direction normal to the wall, and $\mathbf{n}$ is the unit normal vector. Karniadakis *et al.* and related work showed that this 'rotational' boundary condition is superior to the traditional boundary condition,

$$\frac{\partial \Phi}{\partial n} = \frac{2}{Re}\,\mathbf{n}\cdot\nabla^2\mathbf{v}, \tag{18}$$

in that it eliminates the first-order splitting error that Equation (18) introduces.

3.2. Fourier spectral-method

A combined Fourier spectral-method and finite-difference scheme are used to discretize the governing equations since only the radial direction does not have periodic boundary conditions. The three velocity components and the pressure can be expressed in general as functions of time and space,

$$f(r,\theta,z,\tau) = \sum_{l=-L/2}^{L/2-1}\ \sum_{k=-N/2}^{N/2-1} f_{kl}(r,\tau)\,\mathrm{e}^{\mathrm{i}k\theta}\,\mathrm{e}^{\mathrm{i}2\pi lz/Z}, \tag{19}$$

where $\mathrm{i}=\sqrt{-1}$, N and L are the number of collocation points in the circumferential and axial directions respectively, and Z is the length of the computational domain in the axial direction. In these formulae, the terms with $l=-L/2$ or $k=-N/2$ are present because of the fast Fourier transform, which is used extensively in the solution process and requires an even number of terms with which to work.

3.3. Transformed equations

In the radial direction, the co-ordinate transformation,

$$r = \mathrm{e}^{\xi}, \tag{20}$$

is used to generate a finer physical mesh near the wall of the cylinder than further away from it. From now on, the transformed equations and boundary conditions will be in the transformed system of τ, ξ and the Fourier coefficients. The equations to solve in this system are

$$\frac{1}{\alpha}\frac{\hat{\mathbf{v}}_{kl}-\mathbf{v}^{n}_{kl}}{\Delta\tau} = -\frac{1}{2}(3\mathbf{N}^{n}_{kl}-\mathbf{N}^{n-1}_{kl}) + \frac{1}{2}\mathbf{L}^{n}_{kl}, \tag{21}$$

$$\left(\frac{1}{r^2}\frac{\partial^2}{\partial\xi^2}-\frac{k^2}{r^2}-\sigma^2 l^2\right)\Phi^{n+1/2}_{kl} = \frac{(\nabla\cdot\hat{\mathbf{v}})_{kl}}{\alpha\Delta\tau}, \tag{22}$$

$$\frac{1}{\alpha}\frac{\tilde{\mathbf{v}}_{kl}-\hat{\mathbf{v}}_{kl}}{\Delta\tau} = -\left(\frac{1}{r}\frac{\partial}{\partial\xi}\mathbf{e}_r + \mathrm{i}k\mathbf{e}_\theta + \mathrm{i}\sigma l\mathbf{e}_z\right)\Phi^{n+1/2}_{kl} \tag{23}$$

and

$$\frac{1}{\alpha}\frac{\mathbf{v}_{kl}^{n+1}-\tilde{\mathbf{v}}_{kl}}{\Delta\tau}=\frac{1}{2}\mathbf{L}_{kl}^{n+1}, \tag{24}$$

where $-L/2+1\leq l\leq L/2-1$, $-N/2+1\leq k\leq N/2-1$, and $\mathbf{e}_r$, $\mathbf{e}_\theta$ and $\mathbf{e}_z$ are the unit vectors in the radial, circumferential and axial directions respectively.

The calculation of the nonlinear terms in Equation (21) is the most time-consuming part in the computation. First, we need to calculate the Fourier coefficients of velocity and vorticity, then obtain their physical values at the collocation points. The physical values of the nonlinear terms are then obtained at these collocation points. Finally, they are transformed to the wave space to give the Fourier coefficients of the nonlinear terms. The Poisson equation, which usually takes most of the time in finite-difference formulations, is reduced to a system of tridiagonal equations. The operation count for solving the Poisson equation is $O(MNL)$, in contrast to the operation count for the nonlinear terms, which is $O(MNL\log_2(NL))$ when the fast Fourier transform (FFT) is used. The rotational form of the convective terms is chosen because of its stability features in spectral approximations. It also has an advantage over the traditional form $(\mathbf{v}\cdot\nabla\mathbf{v})$ in computational time. The rotational form needs a total of nine FFT operations (one inverse FFT for each of u, v, w, ω_r, ω_θ and ω_z, one FFT for each component of the nonlinear terms) per time step. The traditional form needs a total of 15 (one inverse FFTS for each of the three velocity components and their nine derivatives and one FFT for each of the components of the convective terms) per time step. The utilization of the rotational form of the convective terms thus brings about a significant reduction in computational time.

3.4. Finite-difference scheme

In this study, we use a half-staggered grid, as shown in Figure 1. All of the vector components are determined at the intersection of solid lines, whereas all of the scalars (pressure, divergence, etc.) are defined on points that are the intersections of solid and dashed lines. A half-staggered grid gives the best balance between different factors of concern in the current study. We then have to find the pressure on the wall for the calculation of fluid forces and velocity. Fortunately, the variation of pressure near solid walls is not as steep as that of velocity. Thus, we use an extrapolation procedure, which is based on the pressure values in the flow field and the pressure gradient on the wall, to obtain the wall pressure.

3.5. The pressure equation

For each pair of modes (k, l), the Poisson equation for pressure, Equation (15), or its discrete form, Equation (22), becomes a tridiagonal algebraic equation. The Poisson equation for Φ and the boundary conditions (which are a combination of the Neumann boundary conditions and periodic boundary conditions) cannot uniquely determine Φ, which reflects the lack of thermodynamic meaning of pressure in incompressible flows. In the numerical implementation, the end row of the coefficient matrix of the system of algebraic equations is reduced to all zeros by the forward sweep of the Thomas algorithm for the tridiagonal equation when both k and l are zero. We set the arbitrary constant by setting the Fourier coefficients of the mode $k=l=0$ at the end of the forward sweep ($i=3/2$ in our calculations since the forward sweep is from the outer boundary to the wall of the cylinder) to zero.

3.6. Outflow boundary conditions

Boundary conditions for pressure at the outer boundary are not a trivial issue in the present study, as they may influence the inner flow by the incompressible nature of the fluid.

Development of appropriate boundary conditions for pressure and velocity at the outer boundary, especially at outflow or mixed inflow–outflow boundaries, have been discussed by many researchers, such as Sani and Gresho [11] and Mittal and Balachandar [12]. However, because of the complexity of the problem and the large variation of flow conditions, no widely applicable formulation of boundary conditions at numerically truncated boundaries (open boundaries) is currently available.

The outflow boundary conditions for velocity should be such that the boundary condition should not interfere with the possible outflow passage of vortices and also should not affect the global properties of the flow, such as drag, lift and vortex shedding. For this oscillating flow problem, it is tempting to say that the outer boundaries are sufficiently far from the cylinder so that all of the vortices, i.e., those that exist from previous oscillations and those that are being formed, do not approach the far-field boundary. However, there is no need to make this assumption. We select conditions that will not deform the vortices as they either approach or pass through the far-field boundary. Thus, we use the following conditions for oscillating flows:

$$\frac{\partial^2 u_{kl}}{\partial r^2} = \frac{\partial u_{kl}}{\partial r} = 0, \tag{25}$$

$$\frac{\partial^2 v_{kl}}{\partial r^2} = \frac{\partial v_{kl}}{\partial r} = 0 \tag{26}$$

and

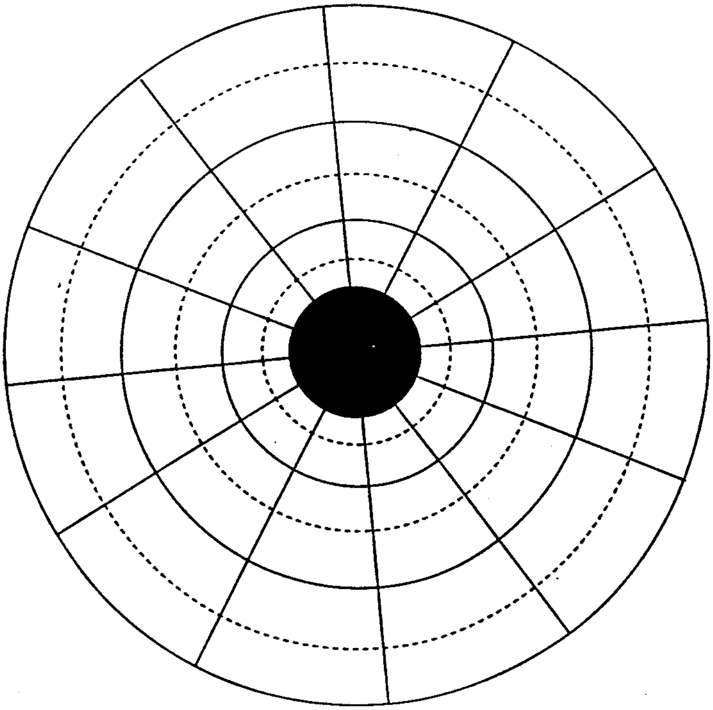

Figure 1. The half-staggered grid in a r, θ plane. The grid system is the same on the r, θ plane for each axial collocation point. Vectors are defined at the intersections of solid lines, and scalars are defined on the intersections of solid and dashed lines.

$$\frac{\partial^2 w_{kl}}{\partial r^2} = \frac{\partial w_{kl}}{\partial r} = 0. \tag{27}$$

These are equivalent to

$$\frac{\partial^2 u_{kl}}{\partial \xi^2} = \frac{\partial^2 \upsilon_{kl}}{\partial \xi^2} = \frac{\partial^2 w_{kl}}{\partial \xi^2} = 0. \tag{28}$$

Both u and υ for $k = 1$, $l = 0$ are specified:

$$u_{1,0} = u_{-1,0} = U_\infty((n+1)\Delta\tau)/2, \tag{29}$$

$$\upsilon_{1,0} = -\upsilon_{-1,0} = U_\infty((n+1)\Delta\tau)/2, \tag{30}$$

where U_∞ is the velocity from Equation (6) at r_∞. For these oscillating flows, the outflow pressure boundary condition is determined from the radial derivative of the pressure as found from the radial component of the momentum equation.

4. CALCULATION OF THE FORCE COEFFICIENTS

The fluid forces acting on the cylinder can be represented by contributions from pressure and shear stress. Unlike the steady approach flow problem, the oscillating flow problem has a significant time-dependent inline force component. Also, the transverse force time-dependency in oscillating flows is quite different since the approach flow never has a constant velocity. However, the inline and transverse forces can still be found from the same equations used in steady flow:

$$C_{\mathrm{f}} = -\frac{1}{Z}\int_0^z \int_0^{2\pi} \left(p\cos\theta + \frac{2}{Re}\,\omega_z \sin\theta\right)_{r=1} \mathrm{d}\theta\,\mathrm{d}z \tag{31}$$

and

$$C_{\mathrm{t}} = -\frac{1}{Z}\int_0^z \int_0^{2\pi} \left(p\sin\theta - \frac{2}{Re}\,\omega_z \cos\theta\right)_{r=1} \mathrm{d}\theta\,\mathrm{d}z, \tag{32}$$

where C_{f} and C_{t} are the inline and transverse force coefficients respectively, Z is the cylinder length, and p and ω_z are evaluated on the cylinder surface. Since both pressure and vorticity are z-dependent, sectional values of both inline and transverse forces can be determined by suppressing the z-integration in Equations (31) and (32) and using z-local distributions of p and ω_z. In an oscillating flow, the drag and inertia coefficients, C_{D} and C_{M}, in the Morison equation are determined by the Fourier integral method. The dimensionless Morison equation for a sinusoidally oscillating flow is

$$C_{\mathrm{F}} = C_{\mathrm{D}}\sin\theta|\sin\theta| + C_{\mathrm{M}}\frac{\pi^2}{\mathrm{KC}}\cos\theta. \tag{33}$$

Equation (33) is multiplied by $\cos\theta$ and integrated to give

$$C_{\mathrm{M}} = \frac{\mathrm{KC}}{\pi^3}\int_0^{2\pi} \cos\theta\, C_{\mathrm{F}}\,\mathrm{d}\theta. \tag{34}$$

Then (33) is multiplied by $\sin\theta$ and integrated to give

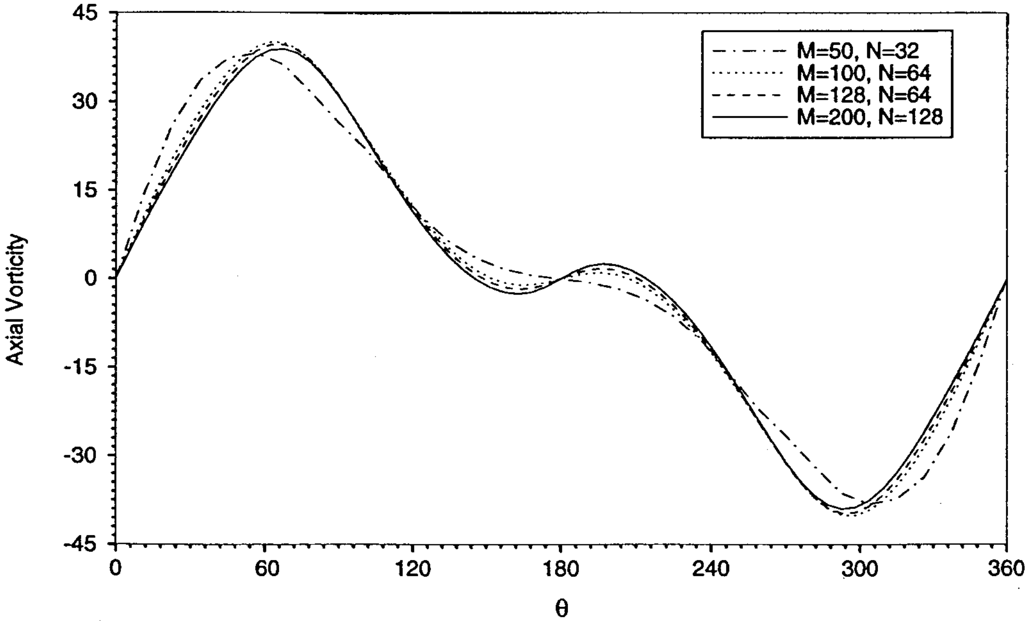

Figure 2. Axial vorticity on the wall of the cylinder for sinusoidally oscillating flow at KC = 2 and $\beta = 196$ with different spatial resolutions. The outer boundary radius is $r_\infty = 42.5$ and the time step is $\Delta\tau = 0.002$.

$$C_D = \frac{3}{8}\int_0^{2\pi} \sin\theta \, C_F \, d\theta. \tag{35}$$

These coefficients will be discussed in the next section.

5. NUMERICAL RESULTS

To demonstrate the capability of the numerical method to calculate the Honji instability, we set β at a value of 196 and let KC range from 1 to 4. The flow is expected to be 2D at the lower end of the KC range and 3D at the upper end, with the viscous transition between 2D and 3D occurring somewhere at about KC = 1.75 [2].

5.1. Convergence and stability

Before discussing the range of calculations undertaken, we present the results of part of the convergence and stability study. We will discuss the case of KC = 2 and $\beta = 196$. This situation is expected to produce a 3D viscous flow, i.e., the Honji instability has occurred, but no turbulence is present yet (see Sarpkaya [2]). We treat the convergence problem in two steps because of the complexity of doing a full 3D convergence test. First, we consider the flow to be 2D and determine the necessary grid for 2D convergence. Second, we take the grid for which we got a 2D convergence and complete the convergence check by varying the number of mesh points in the axial co-ordinate direction.

Four different mesh systems were examined in the 2D part of the study, as indicated in Figure 2, which shows a plot of the surface vorticity distribution for each mesh system. The vorticity distributions at the two finest mesh systems, 128 × 64 and 200 × 128, are virtually the

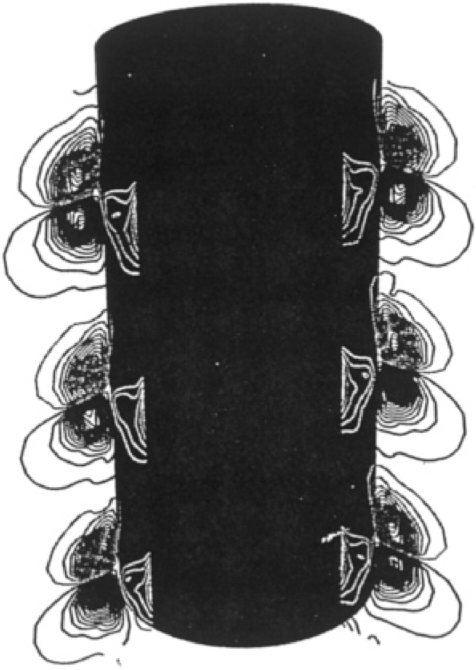

Figure 3. Contour lines of circumferential vorticity at $\tau = 33$ for sinusoidally oscillating flow at $KC = 2$, $\beta = 196$ with $r_\infty = 42.5$, $M = 128$, $N = 64$, $L = 32$ and $\Delta\tau = 0.002$.

same. Therefore, we proceed to the 3D part of the convergence check with the 128×64 2D grid.

The number of axial collocations was allowed to vary for the 128×64 (radial by circumferential) systems. We used 8, 16 and 32 axial points with the $L = 32$ case providing a well-defined axial variation of the circumferential vorticity with a wavelength of about 1.5, which agrees quite well with the experimental values of Honji. The vorticity plot is shown in Figure 3.

Calculations for two different time steps, 0.001 and 0.002, were performed for the $128 \times 64 \times 32$ mesh system. The results, not shown here for brevity, indicate that both time steps produced virtually identical results. In addition, two different outer boundaries, $r_\infty = 20.09$ and 42.5, were examined with $r_\infty = 42.5$ necessary to produce the physically correct drag and inertia coefficients shown in Table I and discussed later. So, we proceed with a $128 \times 64 \times 32$ grid, a time step of 0.002, an outer boundary of 42.5 cylinder radii and a spanwise computational length of 4.5 cylinder radii.

Table I. Drag and inertia coefficients for different KC values at $\beta = 196$

KC	C_D, calc.	C_D, exp.[a]	C_M, calc.	C_M, exp.[a]
1.0	2.06	—	2.15	—
2.0	1.36	1.7	2.05	2.15
2.6	1.11	1.3	2.08	2.08
3.2	1.16	1.25	2.01	2.05
4.0	1.21	1.2	1.97	2.01

[a] [15].

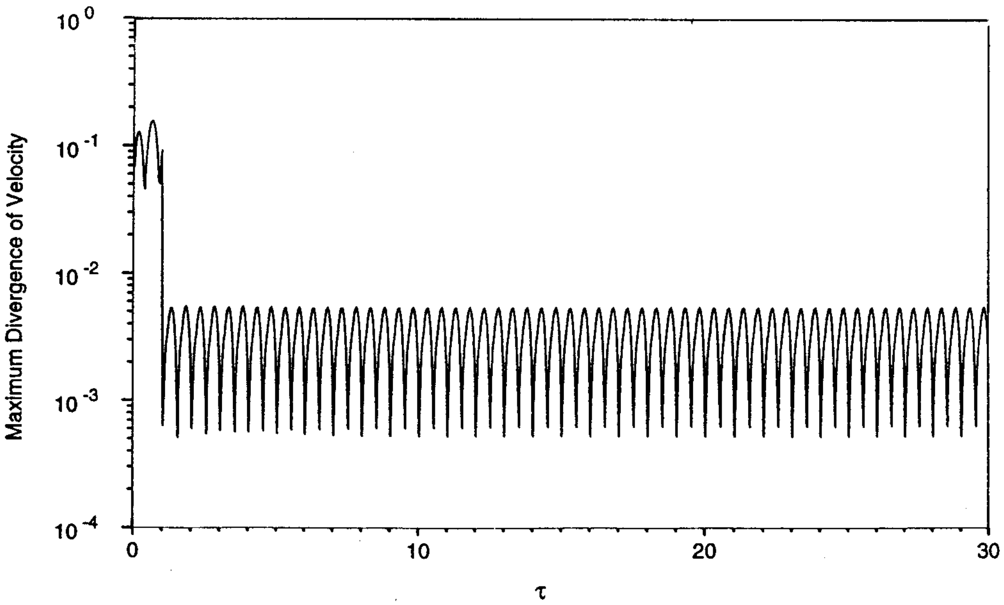

Figure 4. The maximum divergence of velocity for $\mathrm{KC} = 1$ and $\beta = 196$.

The issue of these parameters has been re-examined for the higher KC values in this study. However, only the convergence and stability results for $\mathrm{KC} = 2$ and $\beta = 196$ are presented in this description of the results.

5.2. *KC* $= 1$, $\beta = 196$

Physically, this case is a 2D flow. The calculation will treat the problem as if it were 3D and perturb the velocity components. If the perturbations are damped, the 2D nature of the flow is retained and the onset of the Honji instability will not occur.

We use the $120 \times 64 \times 32$ grid with $\Delta\tau = 0.002$ and $r_\infty = 42.5$. The perturbation to the velocity is applied from $\tau = 0$ to $\tau = 1$. The maximum divergence of the velocity is shown in Figure 4, where it is observed that the divergence is relatively high during the time that the perturbation is applied. After the perturbation was removed, the divergence quickly stabilized to a value oscillating about 2×10^{-3}, which we consider to be satisfactory. After the perturbation is removed at $\tau = 1$, the velocity quickly decreases, oscillating about a zero mean, to a magnitude of approximately 0.0015 after 30 cycles. The isolines of ω_z (not shown) are straight lines, having no z dependence. The decrease of the axial velocity to its expected value of zero and the 2D behavior of ω_z each infer the 2D nature of the flow.

The contour lines of ω_z are shown in Figure 5 at $\tau = 30.5$ (zero velocity) with the black lines indicating positive vorticity and the grey lines negative vorticity. This map of ω_z is the same at all axial positions. Several overlapping regions, the Stokes layer, of alternate sign vorticity are seen; these are due to the oscillating free-stream flow. At zero velocity, the Stokes layer is thicker than at maximum velocity and the outer layer is a full sized layer.

Figure 6 shows the inline and transverse force coefficients. The symmetry of the wake at this low value of KC ($= 1$) is evident in this plot due to the zero transverse force and the purely sinusoidal behavior of the inline coefficient.

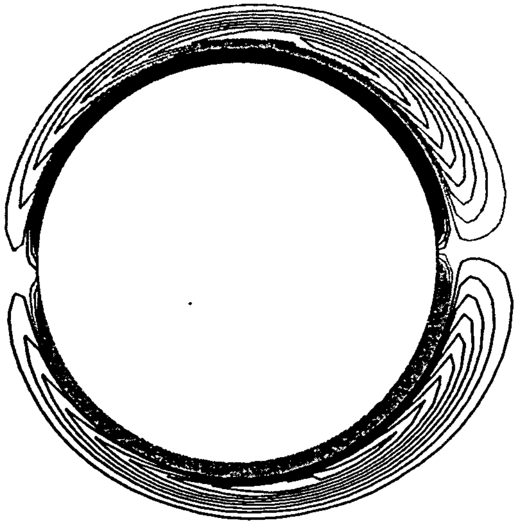

Figure 5. Contours lines for the axial vorticity (ω_z) for KC = 1, $\beta = 196$, and $\tau = 30.5$. The black lines have positive ω_z and the grey lines have negative ω_z.

From the Fourier method applied to the Morison equation, we obtain a drag coefficient of $C_D = 2.06$ and an inertia coefficient of $C_M = 2.15$. The pressure contribution to C_D is 0.99 and the shear stress contribution is 1.07. The inertia coefficient agrees well with the theoretical values of Stokes [13] and Wang [14]. The drag coefficients are a little higher than the Stokes–Wang value of 1.87. We attribute this difference to the nonlinear effect that is fully included in the numerical simulation but was neglected in Stokes and taken as a secondary

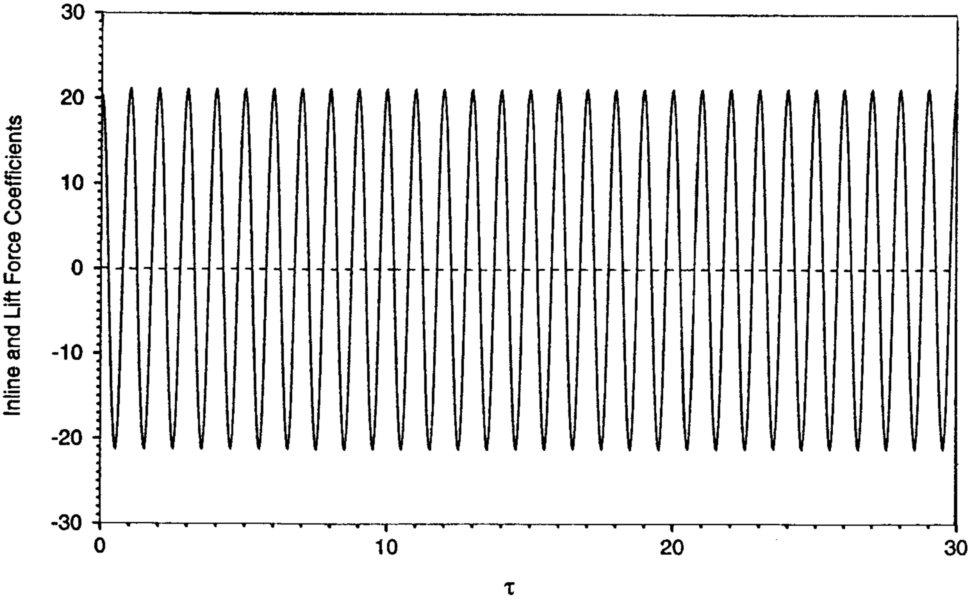

Figure 6. Inline and transverse force coefficients for KC = 1, $\beta = 196$.

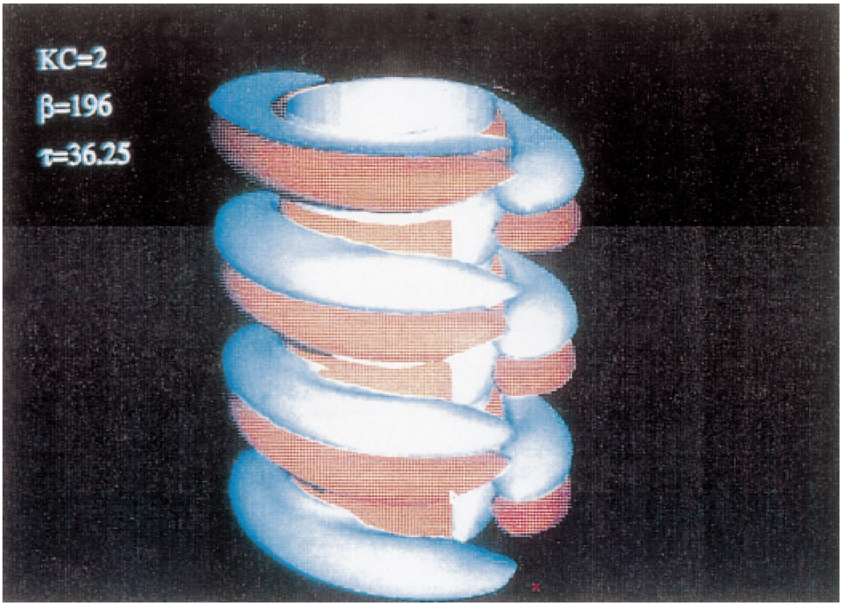

Plate 1. Isosurfaces of ω_θ at $\tau = 36.25$ for $\mathrm{KC} = 2$ and $\beta = 196$; the positive direction of oscillation is the x-direction.

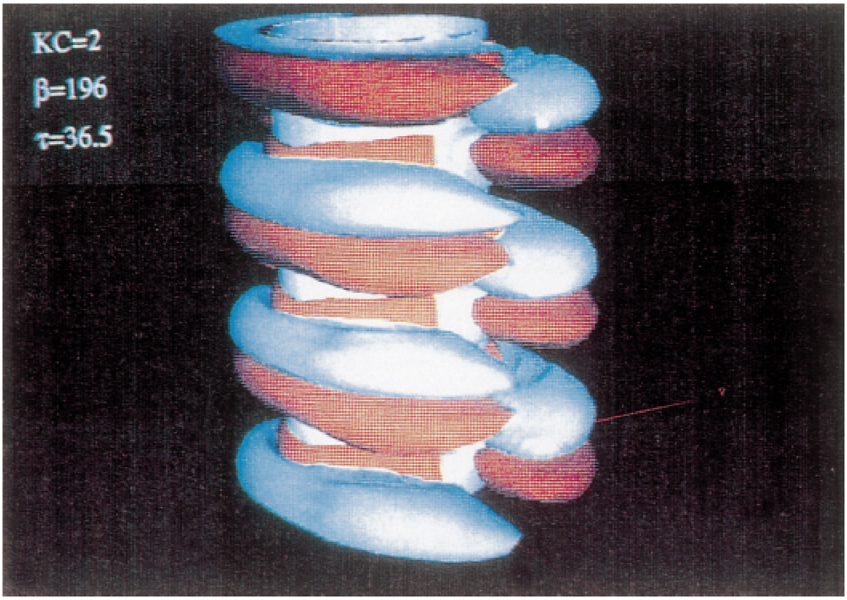

Plate 2. Isosurfaces of ω_θ at $\tau = 36.5$ for $\mathrm{KC} = 2$ and $\beta = 196$; the positive direction of oscillation is the x-direction.

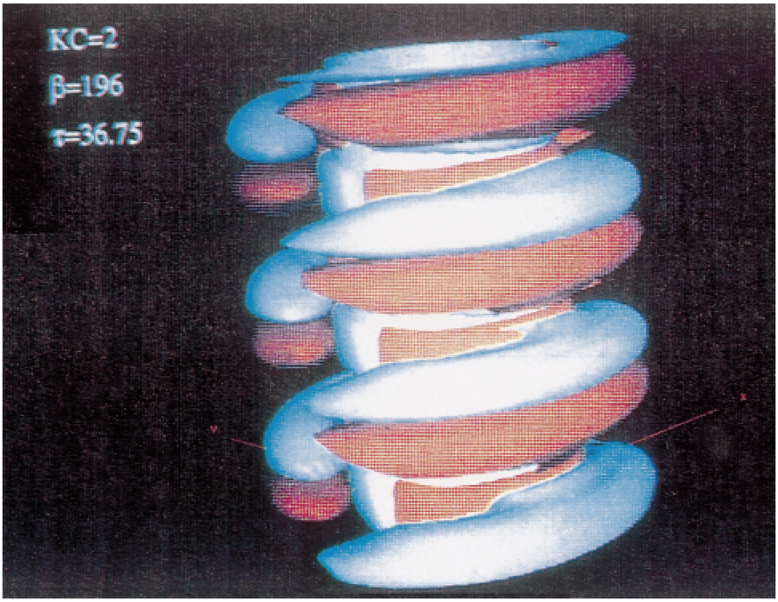

Plate 3. Isosurfaces of ω_θ at $\tau = 36.75$ for KC = 2 and $\beta = 196$; the positive direction of oscillation is the x-direction.

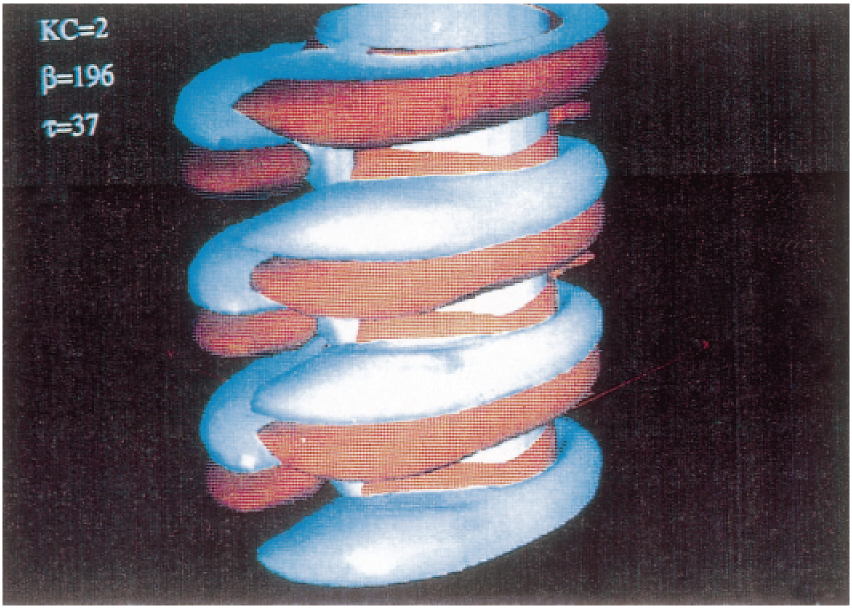

Plate 4. Isosurfaces of ω_θ at $\tau = 37$ for KC = 2 and $\beta = 196$; the positive direction of oscillation is the x-direction.

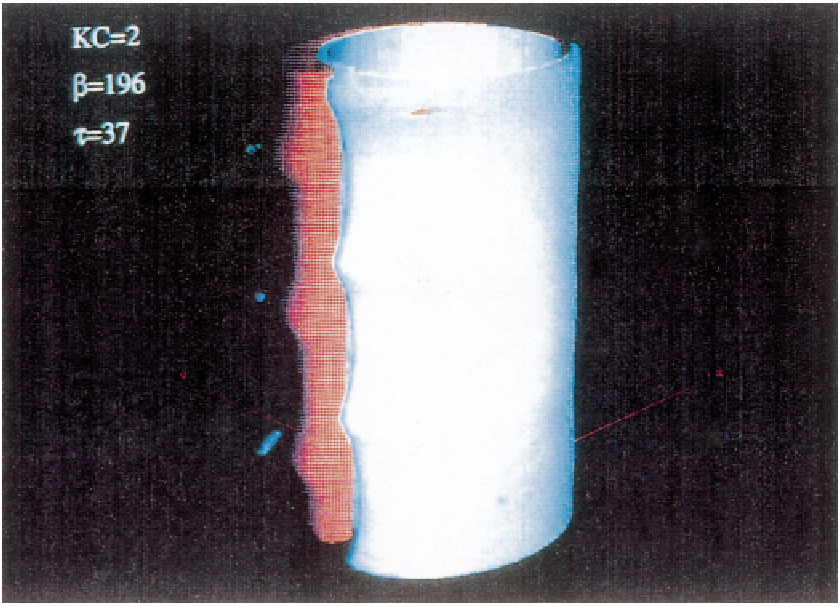

Plate 5. Isosurfaces of ω_z at $\tau = 37$ for $\mathrm{KC} = 2$ and $\beta = 196$; the positive direction of oscillation is the x-direction.

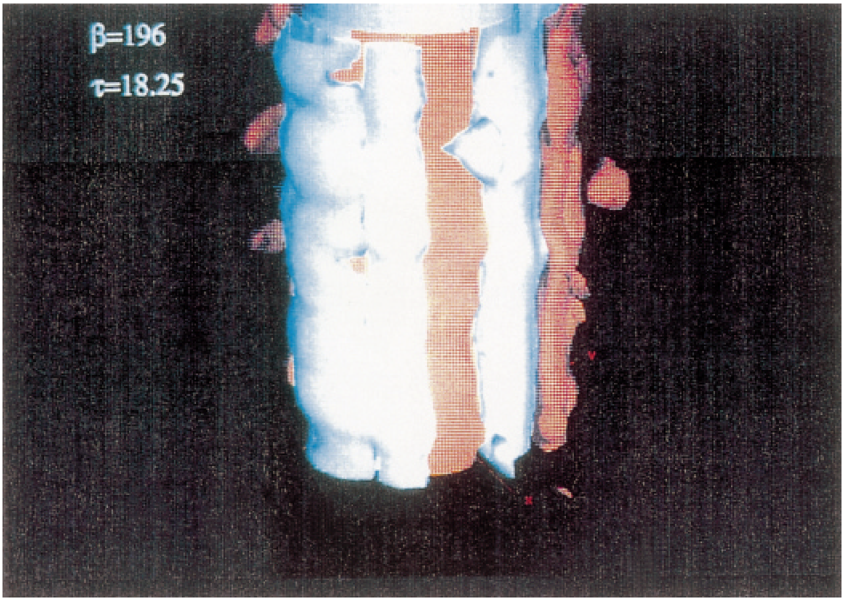

Plate 6. Isosurfaces of axial vorticity for $\mathrm{KC} = 3.2$, $\beta = 196$ and $\tau = 18.25$.

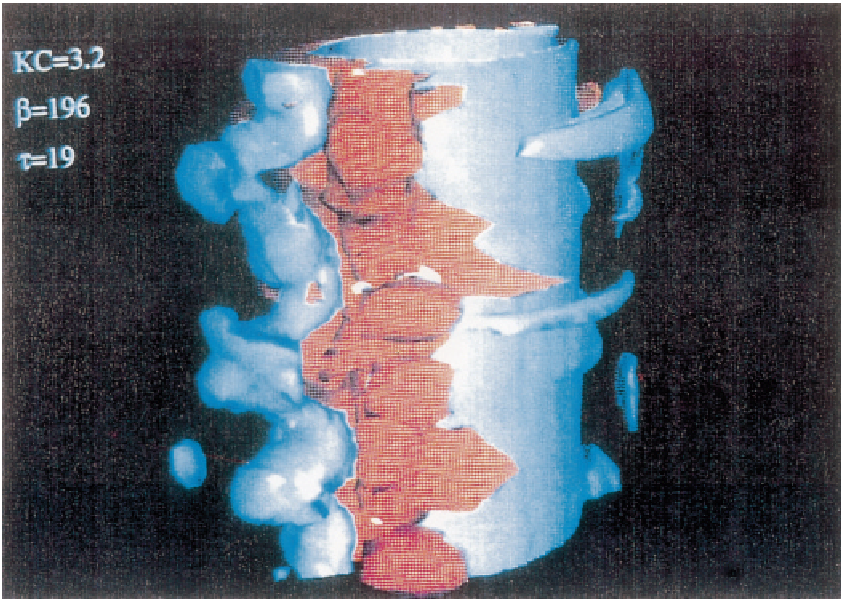

Plate 7. Isosurfaces of axial vorticity for $\mathrm{KC} = 3.2$, $\beta = 196$ and $\tau = 19$.

effect in Wang. Because the flow is inertia-dominated for KC smaller than 4, predicting the inertia coefficient is much easier. This is the reason for the excellent agreement between numerical results and experimental results [15].

5.3. *KC = 2, $\beta = 196$*

When KC is increased to 2 while β remains at 196, the flow becomes unstable to spanwise disturbances. Distinct 3D flow patterns develop and stabilize after about 20 cycles. Plates 1–4 show the isosurfaces of the circumferential vorticity at dimensionless times of 36.25, 36.5, 36.75 and 37. The circumferential component of vorticity is responsible for the development of the mushroom-shaped structures observed by Honji [1] and Sarpkaya [2]. The structures shown in these figures correspond to the outer part of the Stokes layer, although three-dimensionality is present and is spanwise periodic up to the wall. The magnitude of the circumferential vorticity, however, is small compared with the axial component. At $\tau = 37$, the magnitude of ω_θ is 1.7 and the magnitude of ω_z about 36. Therefore, the primary flow pattern is still 2D, as can also be seen from Plate 5 for ω_z at $\tau = 37$. Although several distinct bumps and valleys are clearly seen in the isosurface of ω_z, the flow is dominated by the 2D part. At this KC number, the primary flow is still symmetric and unseparated.

The structures have stabilized after 20 cycles even though this result is not shown here. These structures also keep the same relative locations while moving left and right as the flow direction changes. At peak velocity in the positive direction, Plate 1, the structures are suppressed a little, apparently because of a thinner Stokes layer at peak velocity. When the free-stream velocity decreases to zero and the acceleration of the flow is a maximum, we see slightly expanded structures. This corresponds to the expanded Stokes layer when the velocity is small. The expansion is due to the vortex-induced motion of fluid when the free-stream is weak, as we already observed in the case for KC = 1. When the flow reverses direction, we see a similar behavior of the vortical structures at peak free-stream velocity and peak free-stream acceleration is seen, with reversed directions. In one cycle, the vortical structures do not change location along the span.

The variations of velocity with time in Figure 7 show that the flow becomes almost exactly cyclic after 20 cycles with a period with is the same as the free-stream oscillations. Figure 7 shows that the radial velocity differs very little at the two locations shown. These two locations are not at the same relative points of the axial wave length. Based on this plot and other velocity plots not shown, we conclude that, after they fully develop, the 3D structures become steady in the sense that they do not change locations with flow oscillation at KC = 2 and $\beta = 196$. This is consistent with the observation of Honji [1] that the mushroom-shaped streak sheets stay at the same location along the span after they develop quickly from the start of oscillation.

The axial velocity shown in Figure 8 at two axial positions and at $\theta = \pm\pi/4$ from the positive x-direction. It is quite clear from the velocity results that the axial velocity is not damped and that there is an axial variation in the magnitude and direction of the axial velocity component.

Figure 9 shows the contour lines of axial vorticity (ω_z) at $z = 0$ and at maximum velocity. The symmetry of ω_z is apparent. This plot and others not shown indicate that separation is not occurring even though there is a well-developed Stokes layer. What is missing to infer separation is the presence of a region in which fluid demonstrates an excursion from the wall region [16,17]. This region is not necessarily at the point where ω_z vanishes, i.e., the point where the wall shear stress vanishes, as in a steady approach flow.

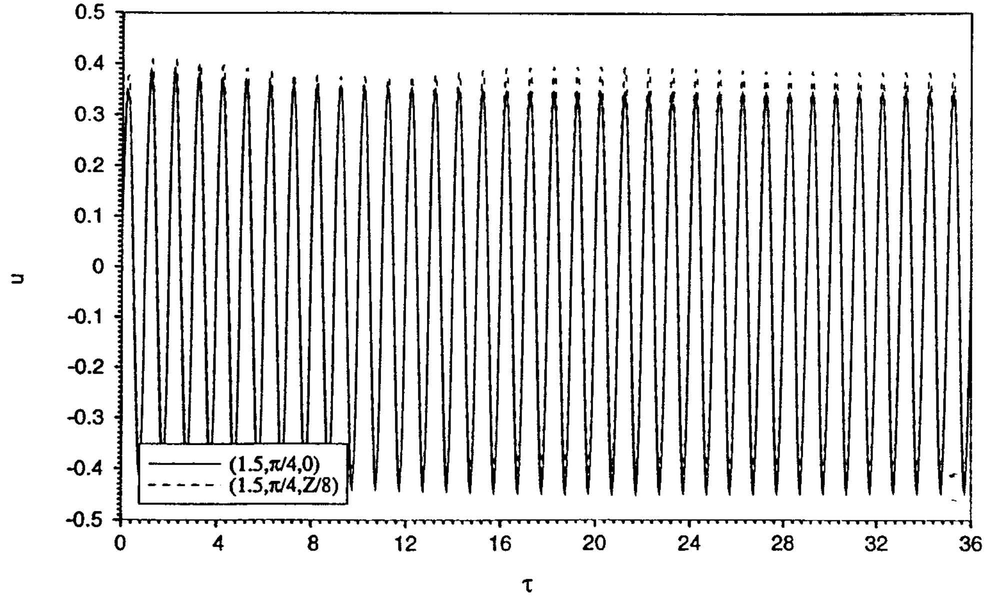

Figure 7. Radial velocity at two different locations along the span. The co-ordinates shown are (r, θ, z); KC $= 2$ and $\beta = 196$.

The length-averaged force coefficient (not shown) was symmetric with a peak of ± 10 at KC $= 2$ and $\beta = 196$. The length-averaged transverse force coefficient (also not shown) was zero as expected because of the symmetry of the flow field. The interesting feature of the transverse force coefficient is that its sectional values (at different z) are different from zero

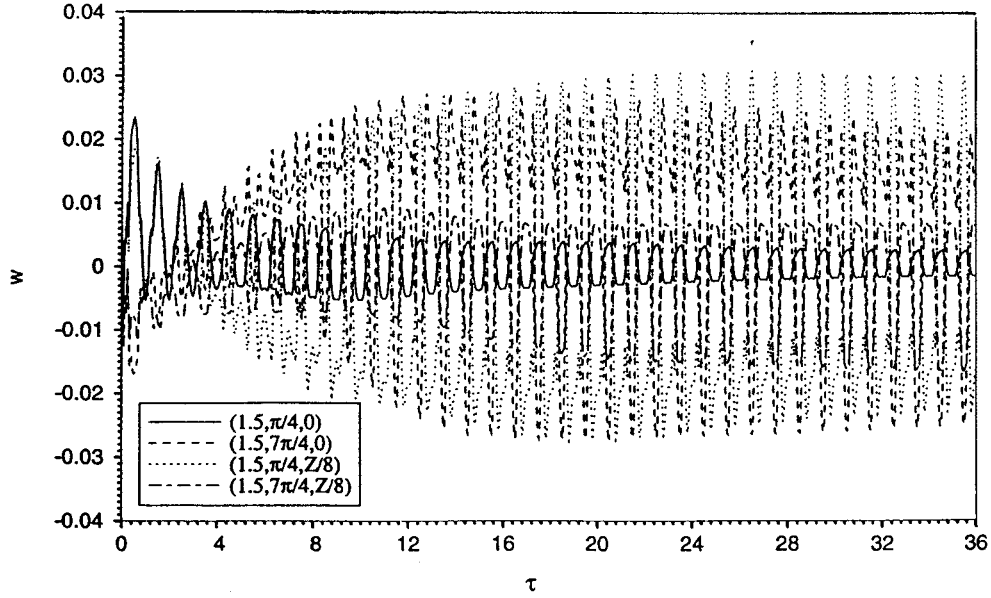

Figure 8. Axial velocity at two locations along the span for KC $= 2$, $\beta = 196$. The co-ordinates shown are (r, θ, z).

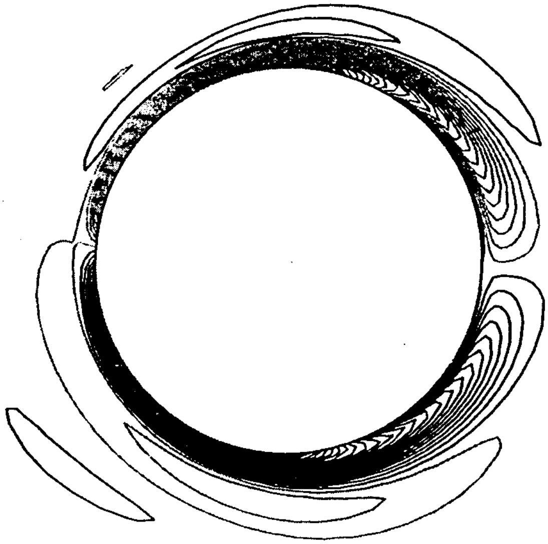

Figure 9. Contours lines for the axial vorticity (ω_z) for KC = 2, $\beta = 196$ and $\tau = 36.25$. The black lines have positive ω_z and the grey lines have negative ω_z.

and, in fact, vary at each of the five axial positions shown in Figure 10. This axial variation of the transverse force coefficient is expected because of the axial variation of the axial component of velocity.

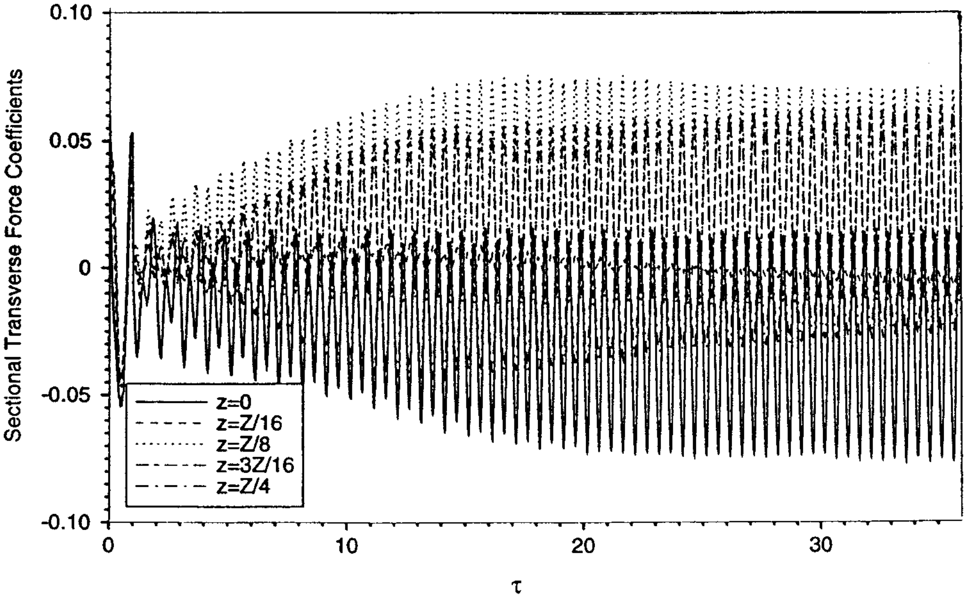

Figure 10. Sectional transverse force coefficients for KC = 2, $\beta = 196$.

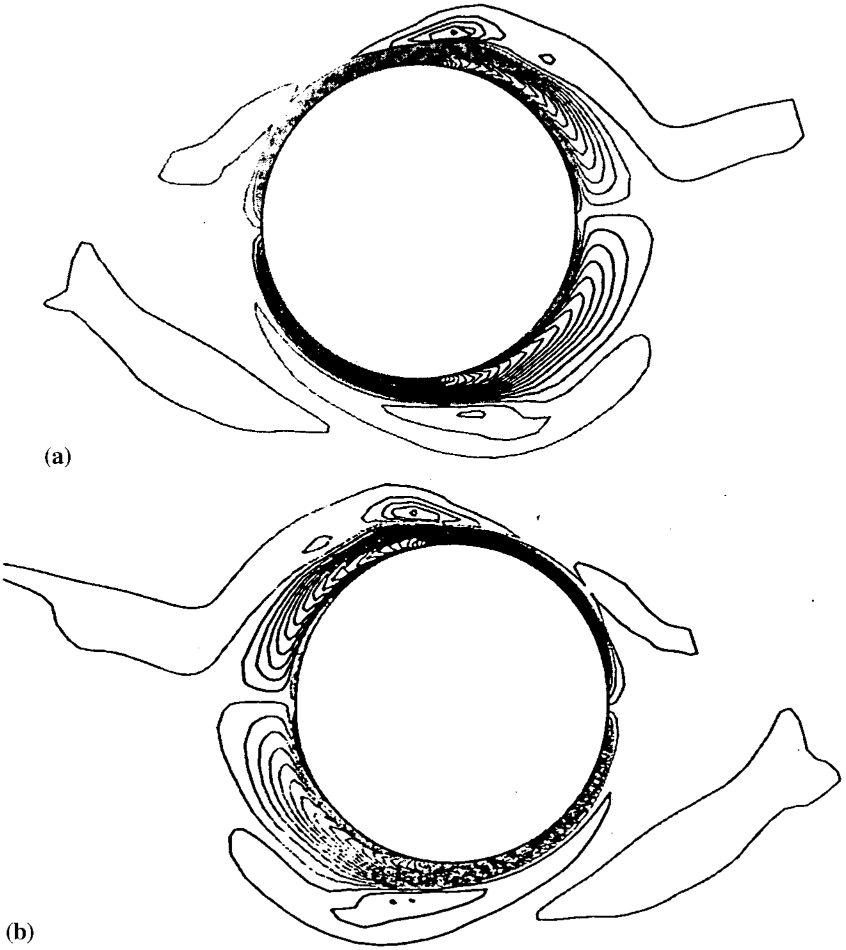

Figure 11. (a) Contours of axial vorticity on the plane $z = 0$, $\mathrm{KC} = 2.6$, $\beta = 196$ and $\tau = 18.25$; (b) contours of axial vorticity on the plane $z = 0$ for $\mathrm{KC} = 2.6$, $\beta = 196$ and $\tau = 18.5$.

5.4. $\mathrm{KC} = 2.6$, $\beta = 196$

Since we learned from the case for $\mathrm{KC} = 2$ and $\beta = 196$ that the initial development of the 3D flow from random numerical perturbations takes about 20 cycles, we use the flow condition at a smaller KC number at the ending time for its calculation as the initial condition for the flow with a higher KC number. A perturbation is applied in the first half cycle of calculation for the higher KC flow so that the computation can select the appropriate flow. From the results we show below, it is clear that the stabilization of the new flow state takes much less time than starting from rest. For $\mathrm{KC} = 2.6$, we use the flow condition of $\mathrm{KC} = 2$ at $\tau = 36$. However, the start of time ($\tau = 0$) for different KC is always at the time the calculation for it begins.

Sarpkaya [2] showed that the flow at separation occurs between KC about 2.1 and 2.5 at $\beta = 196$, and emphasized that accurate determination of separation and transition are both very difficult. In our simulation, we found the Stokes layer is still attached to the cylinder for $\mathrm{KC} = 2.6$ and $\beta = 196$. Figure 11 shows the contour lines of the axial vorticity at $z = 0$ and two different times, $\tau = 18.25$ and 18.75. These two time points represent the maximum velocity of the free-stream flow in both directions. We see, in the downstream part of the cylinder, the axial vorticity on the wall changes sign. For steady flows, the vanishing of surface vorticity (zero shear stress) is the criterion for separation. In unsteady flows, this criterion is not directly applicable. In fact, for $KC = 2$, a similar sign change of the axial vorticity occurs also. Fluid particles that are originally in the Stokes layer remain there. Actually, the sign change just reflects the induced motion of the attached vortices. The region with one sign of vorticity expands as the flow decelerates and takes the full half of the cylinder when the free-stream has maximum acceleration and no velocity (not shown). This phenomenon repeats cycle after cycle while the inner part of the Stokes layer stays attached to the wall and the outer part is detached by the external flow.

The radial and axial velocities at two symmetrical points in the Stokes layer, $r = 1.15$, $\theta = \pi/4$ and $7\pi/4$, and $z = 0$, are plotted in Figure 12(a) and (b). The effect of the perturbation quickly decays and, after about ten cycles of calculation, the new flow state for $KC = 2.6$ is established, and is larger than in the $KC = 2$ case, not only because of stronger vortex motion of the primary flow, but also because of stronger 3D motion. Comparing the radial velocity components in Figures 7 and 12(a) reveals that the asymmetry caused by 3D motion is much stronger at $KC = 2.6$ than for the $KC = 2$ case. A comparison of the axial velocities at the same points from Figures 8 and 12(b) shows the influence of the larger KC value; the asymmetry of the axial velocity is quite evident.

5.5. $KC = 3.2$, $\beta = 196$

With the increase to $KC = 3.2$, the three-dimensionality becomes very strong. The spanwise structures depicted by the isosurfaces of the circumferential vorticity encompass the full flow. At $\tau = 19$, the magnitude of ω_θ is 7.6 while the magnitude for ω_z is 41.5. The relative strength of ω_θ is much larger than the cases with $KC = 2$ and 2.6. The isosurfaces of ω_z at $\tau = 18.25$ (Plate 6) and $\tau = 19$ (Plate 7) further show the strong 3D effects.

At $KC = 3.2$, separation of the Stokes layer occurs. Figure 13 shows that, at $\tau = 18.25$ when the free-stream has the maximum positive velocity, the Stokes layer abruptly deviates from the wall in the downstream part, at both the upper and lower half of the cylinder. When the acceleration of the flow increases to its maximum value, shown in Figure 14, the Stokes layer basically reattaches to the cylinder because of the strong favorable pressure gradient imposed by the free-stream. When the flow reverses directions, the above process repeats itself.

Figures 15 and 16 show the variation of velocity components at $r = 1.15$, $\theta = \pi/4$ and $7\pi/4$, and $z = 0$ with time. Although these two points are well within the Stokes layer, very strong three-dimensionality is present at these points. The axial velocity is of the same order of magnitude as the radial velocity (not shown). The variation of velocity with time is also much more complex than the unseparated flow cases. The flow is generally cyclic, but obvious differences exist between cycles that follow each other, apparently due to vortex-induced velocity effects.

Although three-dimensionality is stronger and separation is present for $KC = 3.2$ and $\beta = 196$, the flow is still primarily 2D and inertia-dominated. As Sarpkaya [2] pointed out, the minimum drag coefficient occurs at a KC value that corresponds to separation. The data of Bearman *et al.* [15] also show this phenomenon. In the current numerical simulations, the minimum drag coefficient (1.11) occurs at $KC = 2.6$. The drag coefficient at $KC = 3.2$ is 1.16, which is very close to the minimum value. Because it is too expensive computationally to simulate many cases with small increments of KC so that a precise minimum can be determined, and also because the range of uncertainly of the KC value corresponding to the minimum drag is only 0.6, we choose not to determine precisely the minimum drag coefficient and the corresponding KC. However, it is clear that the minimum drag is closely related to separation. After separation, the wider unsteady wake induces a larger pressure drag and higher dissipation rate, thus drag will increase. At KC = 3.2, the pressure contribution to C_D

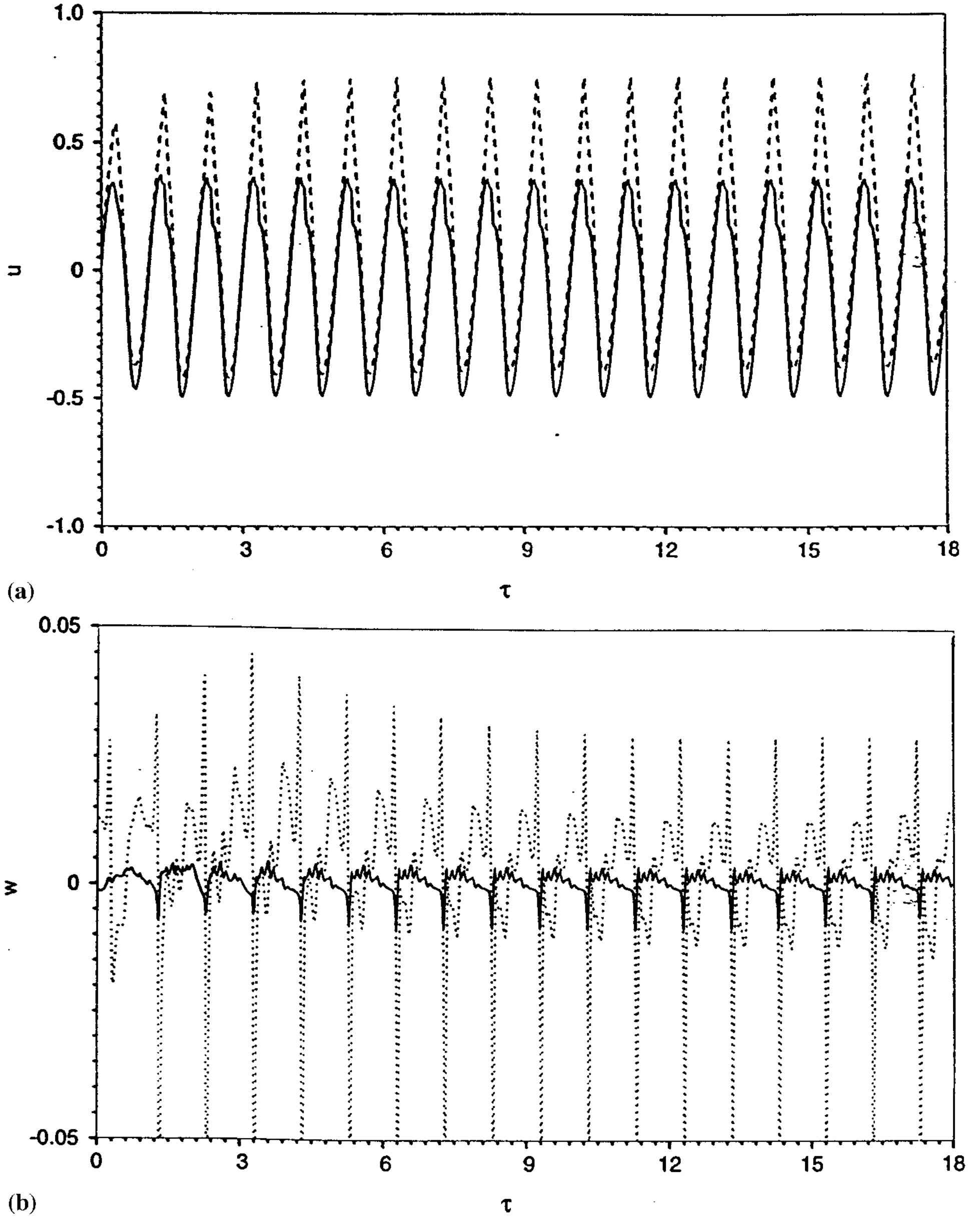

Figure 12. (a) Radial velocity at two symmetrical points $r = 1.5$, $\theta = \pi/4$ (solid line) and $7\pi/4$, and $z = 0$ for KC = 2.6 and $\beta = 196$; (b) axial velocity at two symmetrical points $r = 1.5$, $\theta = \pi/4$ (solid line) and $7\pi/4$, and $z = 0$ for KC = 2.6 and $\beta = 196$.

Figure 13. Contour lines for axial vorticity at the plane $z = 0$ for $\mathrm{KC} = 3.2$, $\beta = 196$ and $\tau = 18.25$. Black and grey lines represent positive and negative ω_z respectively.

is 0.81 and the shear stress contribution is 0.35. The inertia coefficient is 2.01 with a pressure contribution of 1.93 and a shear stress contribution of 0.08.

5.6. $KC = 4$, $\beta = 196$

The flow at $\mathrm{KC} = 4$ varies chaotically in time, while small wavelengths in space become important. The physical flow at $\mathrm{KC} = 4$ is already turbulent. The resolution we use in the

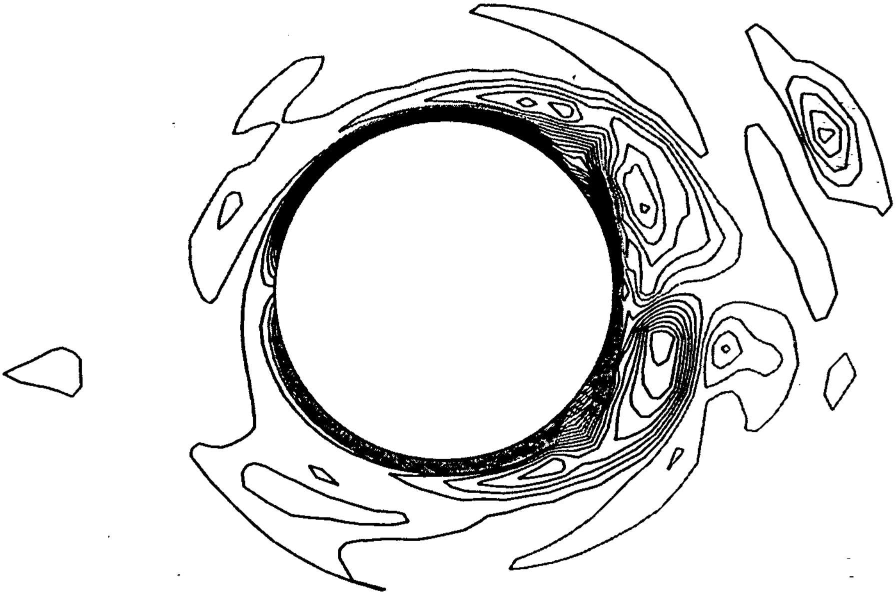

Figure 14. Same as Figure 13 except for $\tau = 18.5$.

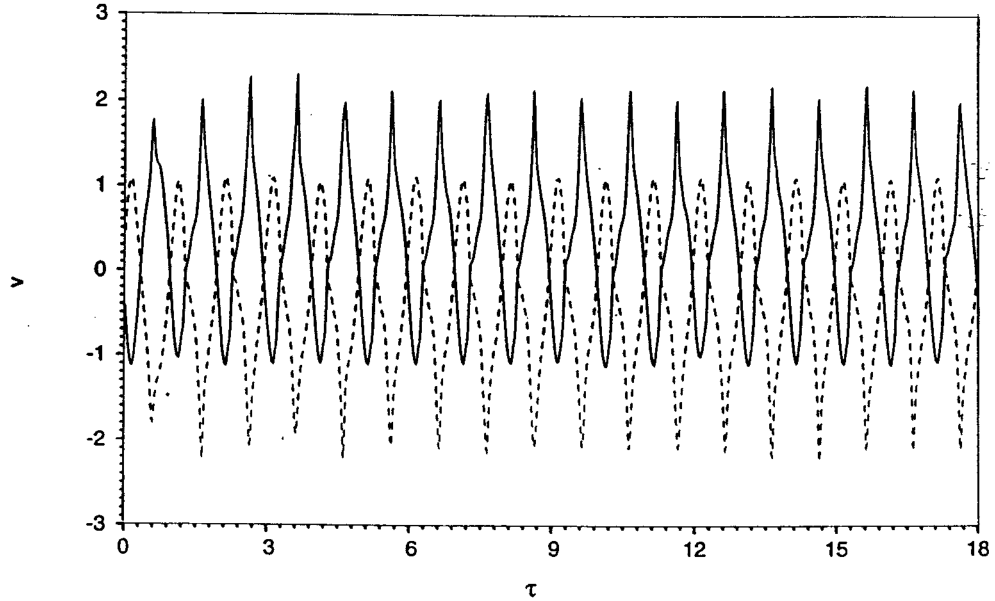

Figure 15. Variation of circumferential velocity with time at two symmetrical locations, $r = 1.15$, $\theta = \pi/4$ (solid line) and $7\pi/4$, and $z = 0$ for KC = 3.2 and $\beta = 196$.

calculations was not enough to resolve the whole range of scales in turbulence. However, we believe that the results still show some key features of the transition process, such as the generation of smaller and smaller spatial and temporal scales.

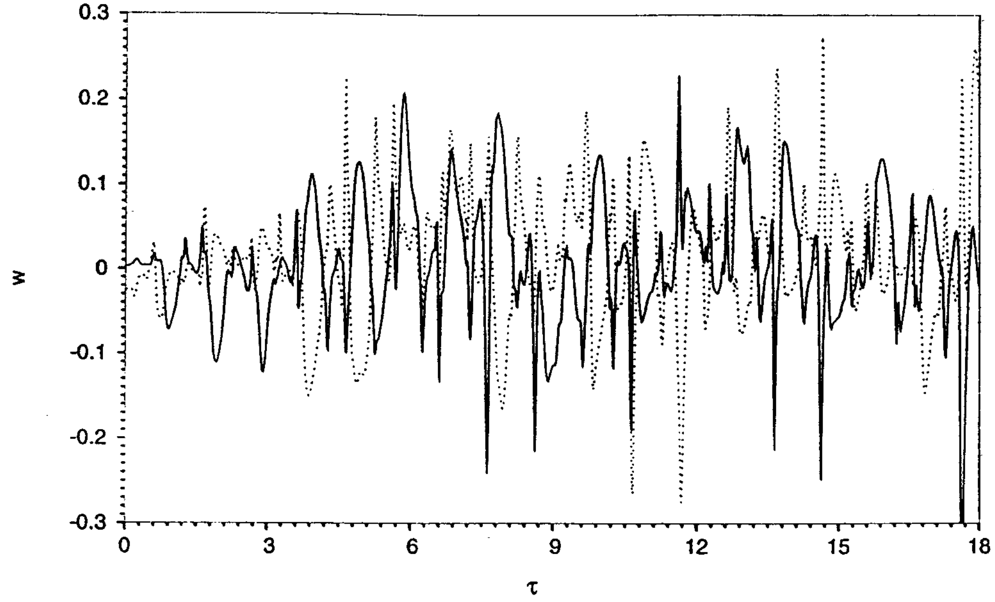

Figure 16. Variation of axial velocity with time at two symmetrical locations, $r = 1.15$, $\theta = \pi/4$ (solid line) and $7\pi/4$, and $z = 0$ for KC = 3.2 and $\beta = 196$.

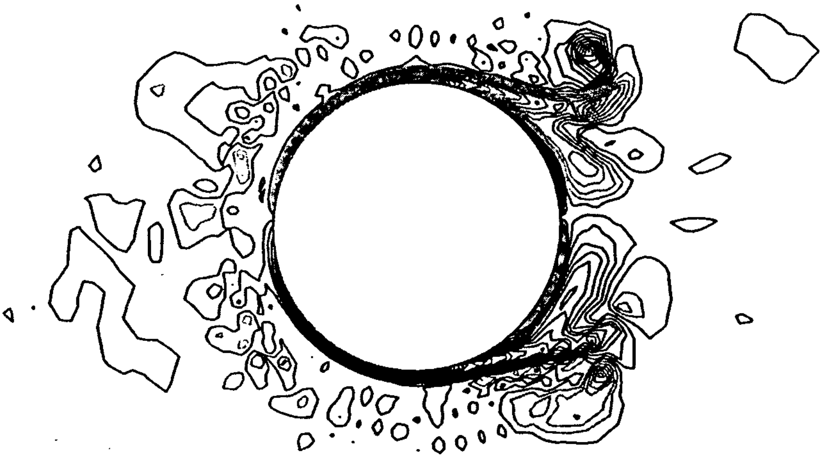

Figure 17. Contour lines for axial vorticity at the plane $z = 0$ for KC = 4, $\beta = 196$ and $r = 18.25$.

Figure 17 shows the contours of axial vorticity at the plane $z = 0$ at two instants in time. Separation is now very obvious at the time of maximum free-stream velocity. At the time of maximum free-stream acceleration, separation is as fully suppressed as in the case for KC = 3.2. Very noticeable small structures are present away from the cylinder. These structures are present both because the spatial resolution is not adequate for this flow, and thus numerical oscillations occur, and because at KC = 4, smaller spatial structures are a physical reality. Since the larger vortices do not have numerical breakdown, we believe the numerical results still reasonably well represent the large scales of the flow.

The temporal variation of velocity is greater and more irregular than for the KC = 3.2 case. There is evidence of a higher harmonic present in the θ-component of velocity at KC = 4, compared with KC = 3.2 case, as shown in Figure 18(a). The axial velocity is shown in Figure 18(b) where the magnitude of the peaks is seen to have increased by a factor of about three when KC increased to 4 from 3.2.

The inline and transverse force coefficients are shown in Figure 19, where the beginning of a transverse force is evident. The difference in inline force at four different equally spaced axial positions is negligible both in magnitude and phase (although this is not shown here). The inline force at KC = 4 is primarily due to pressure with the pressure contribution, the inline force coefficient peaking at about 4.8 and the shear stress contribution peaking at about 0.32. Since the flow is still in the inertia-dominated range, the variation of the inline force is essentially sinusoidal. The drag coefficient is 1.21, compared with the value of 1.5 from Bearman *et al.* [15]. The pressure contribution is 0.93 and the shear stress contribution is 0.28. The inertia coefficient is 1.97, compared with the value of 2.0 from Bearman *et al.*, with the pressure contribution at 1.89 and the shear stress contribution at 0.08.

Table I shows how the calculated values of drag (C_D) and inertia (C_M) coefficients compare with the experimental values of Bearman *et al.* [15]. Very good agreement between the calculated and experimental values is noted for the three highest values of KC. At KC = 2, the inertia coefficients compare reasonably well but the calculated drag coefficient is about 20% lower than the experimental value.

6. SUMMARY

This representation of a sinusoidal flow has allowed the capture of the 3D development of the flow as the value of KC increases from 1 to 4 at $\beta = 196$.

When KC = 1, the flow is 2D, agreeing well with experimental observations. Clear spanwise structures, which are pairs of counter-rotating circumferential vorticity structures, develop at KC = 2. These structures are close to the cylinder and periodic along the span with a

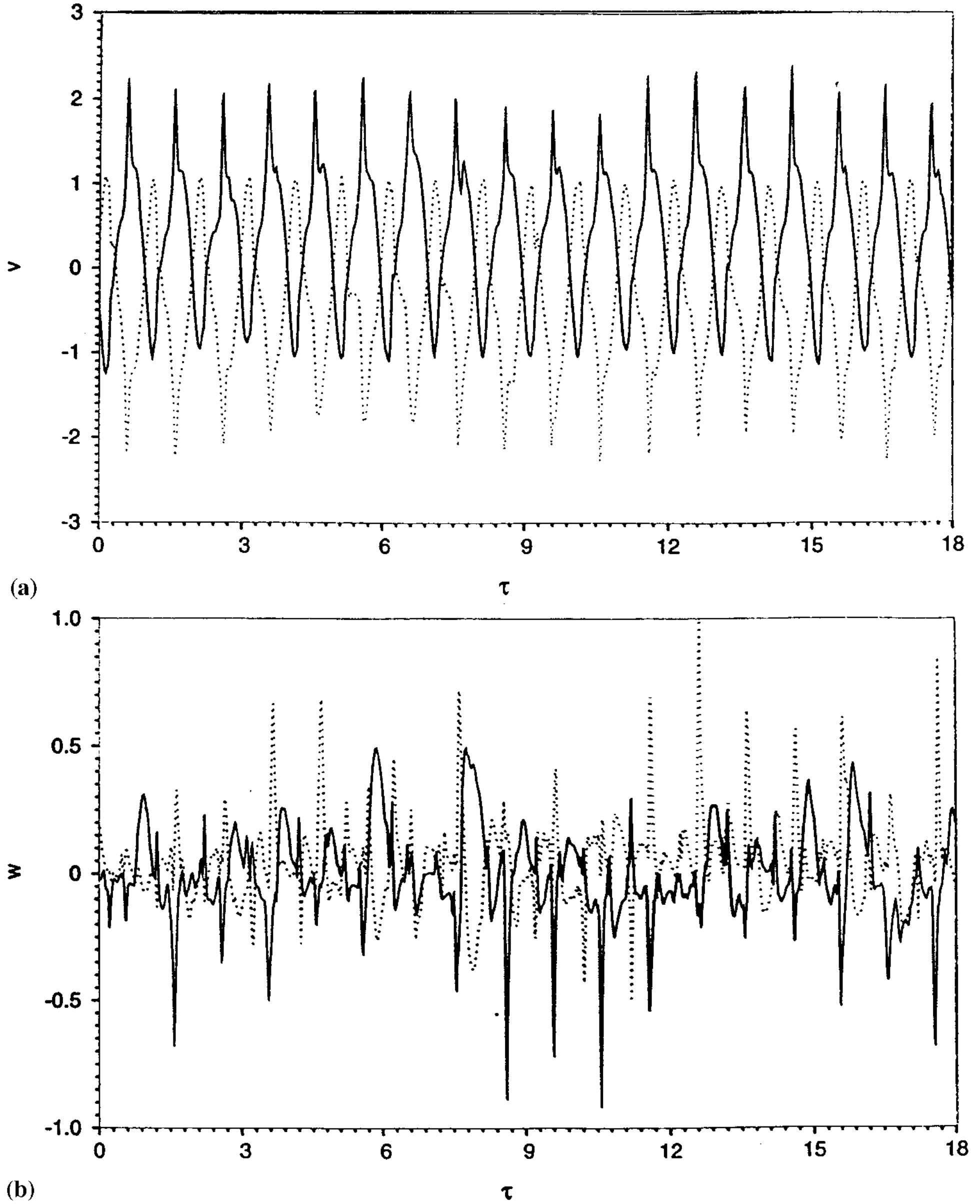

Figure 18. (a) Variation of circumferential velocity at $r = 1.15$, $\theta = \pi/4$ and $z = 0$ with time for KC = 4 and $\beta = 196$; (b) same as (a) except for axial velocity.

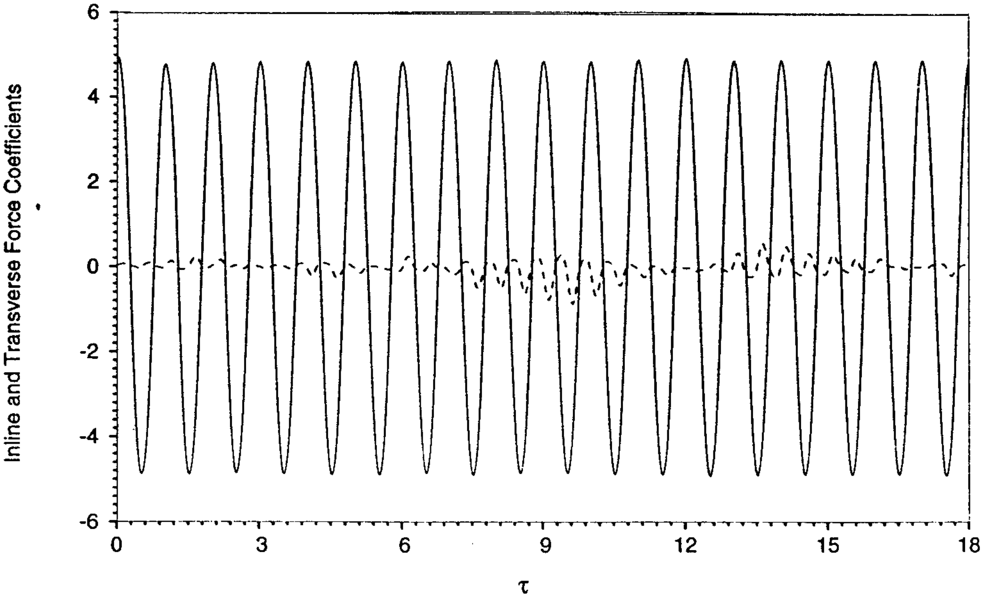

Figure 19. Inline and transverse force coeffiicients for $\mathrm{KC} = 4$ and $\beta = 196$.

wavelength of about 0.75 diameter. These structures do not change locations along the span with time, although they expand or extract with changing free-stream velocity. The centers of the pairs appear on the cross-stream sides of the cylinder alternatively, which explains the alternative mushroom-shaped streak sheets observed when the Honji instability occurs. When KC is increased to 2.6, the three-dimensionality is stronger and the spanwise structures extend into the external flow along the direction of oscillating. For both $\mathrm{KC} = 2$ and 2.6, the primary flow is close to symmetrical in the direction of oscillation, and separation is not present for these flows.

The spanwise structures are not as distinctly shaped for $\mathrm{KC} = 3.2$ as for flows with the two smaller KC numbers. More spanwise modes with shorter wavelengths and more temporal modes with both superharmonics and subharmonics appear. Separation of the Stokes layer occurs and C_D has the minimum value among the flows studied. This confirms the experimental observations that the minimum value of C_D is when separation occurs. We attribute the reason to an increased pressure difference and higher viscous dissipation because of the expansion of the area of vortical activities associated with the occurrence of separation.

The flow at $\mathrm{KC} = 4$ is in an almost chaotic state with a wide range of temporal modes present. Separation is more obvious and the drag coefficient is higher than at $\mathrm{KC} = 3.2$. The spanwise structures are not regular either along the span or with time. More modes with smaller spanwise wavelengths appear. The intermittent increase of velocity is more frequent than the flow at $\mathrm{KC} = 3.2$. It is concluded that the picture of transition to turbulence is the following: the three-dimensionality of the flow generates regions in the flow with concentrated vortices in some part of a cycle of oscillation. With higher KC, these localized and intermittent regions become stronger and last longer. These regions occur first at the outer part of the viscous region, and the reversing of flow induces fluctuations in the inner part of the viscous region. For KC high enough, the fluctuations of velocity become chaotic and the flow undergoes transition to turbulence in the regions of concentration of vorticity. Finally, when

KC is even higher, the turbulent spots are sustained for the whole cycle of oscillation and turbulence transition is induced in the other part viscous region. Flow reversal will probably induce transition of the inner part of the viscous region at about the same time as the outer part. This is different from the steady approach flows, where the wake becomes turbulent at *Re* about 400 and the boundary layer is laminar until *Re* about 2×10^5.

On a loose sense of average over the span of the cylinder, the flows up to $\mathrm{KC} = 4$ are all symmetric. The total transverse force coefficient is very close to zero for $\mathrm{KC} < 4$. For $\mathrm{KC} = 4$, a small transverse force is generated and is present for several cycles. The transverse force vanishes and then reappears for several more cycles and then vanishes again. There is apparently a long term modulation causing this effect. However, this was not examined further. The difference in the sectional transverse force coefficients is present when the Honji instability occurs and the coefficients increase in magnitude with increasing KC. Corresponding to the small transverse force, there is no vortex shedding for these flows.

ACKNOWLEDGMENTS

We are grateful to NSF for Grant ID INT924844 and to the Pittsburgh Supercomputing Center for Grant CBT91004P used in support of this project. They also appreciate helpful discussions with Professor Lixian Zhuang (of the University of Science and Technology of China) who spent a sabbatical with them in Houston.

REFERENCES

1. H. Honji, 'Streaked flow around an oscillating circular cylinder', *J. Fluid Mech.*, **107**, 509–520 (1981).
2. T. Sarpkaya, 'Force on a circular cylinder in viscous oscillatory flow at low Keulegan–Carpenter numbers', *J. Fluid Mech.*, **165**, 61–71 (1986).
3. D. Barkley and R.D. Henderson, 'Three-dimensional Floquet stability analysis of the wake of a circular cylinder', *J. Fluid Mech.*, **322**, 215–241 (1996).
4. A. Roshko, 'On the development of turbulent wakes from vortex streets', *NACA Rep. No. 1191*, 1954.
5. F.R. Hama, 'Three-dimensional vortex pattern behind a circular cylinder', *J. Aerosp. Sci.*, **24**, 156–157 (1957).
6. C.H.K. Williamson, 'The existence of two stages in the transition to three-dimensionality of a cylinder wake', *Phys. Fluids*, **31**, 3165–3168 (1988).
7. C.H.K. Williamson, 'Three-dimensional wake transition', *J. Fluid Mech.*, **328**, 345–407 (1996).
8. M. Thompson, K. Hourigan and J. Sheridan, 'Three-dimensional instabilities in the wake of a circular cylinder', *Exp. Therm. Fluid Sci.*, **12**, 190–196 (1996).
9. P. Hall, 'On the stability of the unsteady boundary layer on a cylinder oscillating transversely in a viscous fluid', *J. Fluid Mech.*, **146**, 347–367 (1984).
10. G.E. Karniadakis, M. Israeli and S.A. Orszag, 'High-order splitting methods for the incompressible Navier–Stokes equations', *J. Comput. Phys.*, **59**, 308–323 (1991).
11. R.L. Sani and P.M. Gresho, 'Resume and remarks on the open boundary condition minisymposium', *Int. J. Numer. Methods Fluids*, **18**, 983–1008 (1994).
12. R. Mittal and S. Balachandar, 'Study of flow over an elliptic cylinder using a direct numerical simulation', *Turbul. Complex Flows, ASME*, **203**, 11–19 (1994).
13. G.G. Stokes, 'On the effect of the internal friction of fluids on the motion of pendulums', *Trans. Cambridge Philos. Soc.*, **9**, 8–106 (1851).
14. C.-Y. Wang, 'On high-frequency oscillating viscous flows', *J. Fluid Mech.*, **32**, 55–68 (1968).
15. P.W. Bearman, M.J. Downie, J.M.R. Graham and E.D. Obasaju, 'Forces on cylinders in viscous oscillatory flow at low Keulgan–Carpenter numbers', *J. Fluid Mech.*, **154**, 337–356 (1985).
16. S. Taneda, 'Definition of separation', *Reports of Research Institute for Applied Mechanics*, vol. 28, Kyushu University, 1980, pp. 73–81.
17. T. Sarpkaya and W. Butterworth, 'Separation points on a cylinder in oscillating flow', *Proc. 10th Int. Conf. Offshore Mechanics and Arctic Engineering*, vol. 1A, The Hague, Netherlands, 1991, pp. 9–18.